Cell Reports
Physical Science

CellPress
OPEN ACCESS

Article

Layer-by-layer delithiation during lattice collapse as the origin of planar gliding and microcracking in Ni-rich cathodes

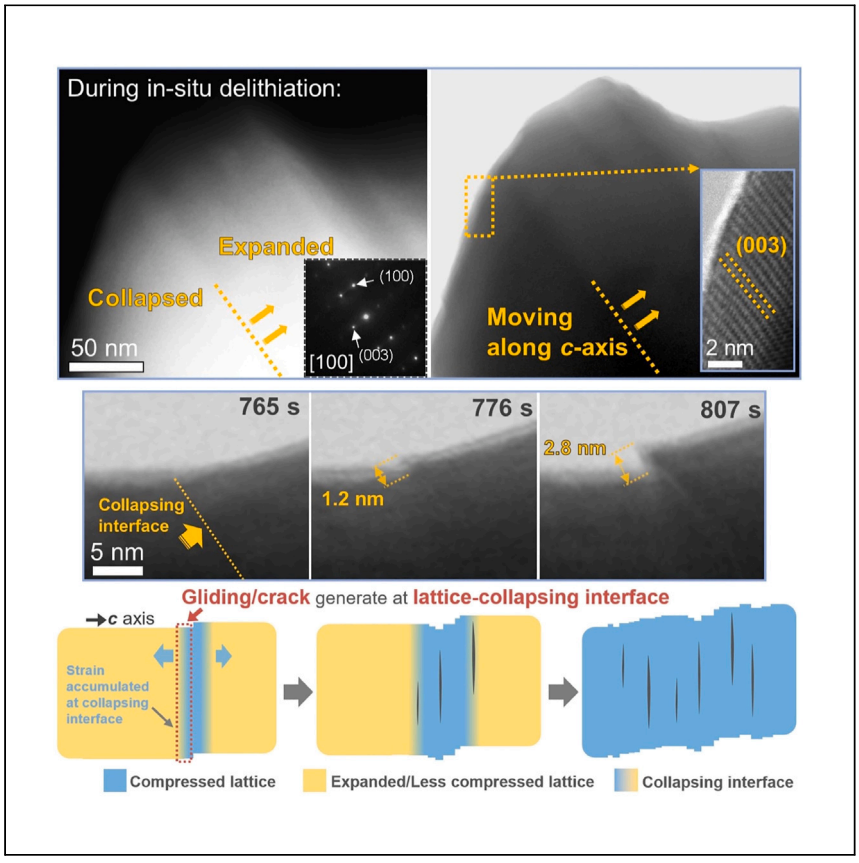

The capacity-fading mechanism for commercialized Ni-rich cathodes is largely unclear. Here, Yu et al. observe the dynamic lattice-collapse process in Ni-rich cathode during delithiation through *in situ* transmission electron microscopy. On the basis of these observations, they propose a "layer-by-layer delithiation" mechanism as the origin of mechanical instability in Ni-rich cathodes.

Ruohan Yu, Weihao Zeng, Liang Zhou, Gustaaf Van Tendeloo, Liqiang Mai, Zhenpeng Yao, Jinsong Wu

mlq518@whut.edu.cn (L.M.)
z.yao@sjtu.edu.cn (Z.Y.)
wujs@whut.edu.cn (J.W.)

Highlights

Dynamic lattice-collapse process of Ni-rich cathode is observed

Lattice collapse is consecutive

Direct observation of defects generated at "collapsing interface"

Mechanical instability originates from "layer-by-layer delithiation"

Yu et al., Cell Reports Physical Science 4, 101480
July 19, 2023
https://doi.org/10.1016/j.xcrp.2023.101480

Cell Reports
Physical Science

CellPress
OPEN ACCESS

Article

Layer-by-layer delithiation during lattice collapse as the origin of planar gliding and microcracking in Ni-rich cathodes

Ruohan Yu,[1,2] Weihao Zeng,[1,2] Liang Zhou,[1] Gustaaf Van Tendeloo,[2,3] Liqiang Mai,[1,*] Zhenpeng Yao,[4,5,6,*] and Jinsong Wu[1,2,7,*]

SUMMARY

High-energy-density nickel (Ni)-rich cathode materials are used in commercial lithium (Li)-ion batteries for electric vehicles, but they suffer from severe structural degradation upon cycling. Planar gliding and microcracking are seeds for fatal mechanical fracture, but their origin remains unclear. Herein, we show that "layer-by-layer delithiation" is activated at high voltages during the charge process when the "lattice collapse" (a characteristic high-voltage lattice evolution in Ni-rich cathodes) occurs. Layer-by-layer delithiation is evidenced by direct observation of the consecutive lattice collapse using *in situ* scanning transmission electron microscopy (STEM). The collapsing of the lattice initiates in the expanded planes and consecutively extends to the whole crystal. Localized strain will be induced at lattice-collapsing interface where planar gliding and intragranular microcracks are generated to release this strain. Our study reveals that layer-by-layer delithiation during lattice collapse is the fundamental origin of the mechanical instability in single-crystalline Ni-rich cathodes.

INTRODUCTION

High-energy-density cathodes are critical in the development of next-generation lithium (Li)-ion batteries (LIBs), particularly for applications such as long-range electric vehicles. As nickel (Ni) is an effective redox participant, the Ni-rich $LiNi_xCo_yMn_{1-x-y}O_2$ (NCM) cathodes have attracted much attention for their high capacity (~200 mAh g^{-1}), high-rate capability, and reduced cost.[1,2] Ni-rich cathodes are always delithiated at high voltage for high power density and maximum Li use. However, severe structural degradation occurring at high voltage has limited their practical applications. Like other layered cathodes, Ni-rich electrodes suffer from several possible structural degradations, such as layered to spinel or rock salt phase transformations,[3] passivation layer formation,[4] and active material dissolution.[5] These degradations usually appear on the surface, and many efforts including coating techniques and other surface treatments[6,7] have been made to mitigate them. Furthermore, Ni-rich cathodes also experience mechanical degradations arise within the grains, where planar gliding[8–10] and intragranular microcracks[11,12] have been observed, and they are usually associated with strain induced by the Li-ion concentration gradient during Li extraction/insertion.[13–17]

Ni-rich NCM cathodes undergo a characteristic anisotropic lattice evolution during electrochemical cycling; a lattice expansion along the *c*-direction and a shrinkage along the *a* and *b* directions are noticed when Li ions are first extracted from the

[1]State Key Laboratory of Advanced Technology for Materials Synthesis and Processing, Wuhan University of Technology, Wuhan 430070, China

[2]Nanostructure Research Center, Wuhan University of Technology, Wuhan 430070, China

[3]EMAT (Electron Microscopy for Materials Science), University of Antwerp, Antwerp, Belgium

[4]Center of Hydrogen Science, Shanghai Jiao Tong University, Shanghai 200240, China

[5]State Key Laboratory of Metal Matrix Composites, School of Materials Science and Engineering, Shanghai Jiao Tong University, Shanghai 200240, China

[6]Innovation Center for Future Materials, Zhangjiang Institute for Advanced Study, Shanghai Jiao Tong University, Shanghai 201203, China

[7]Lead contact

*Correspondence: mlq518@whut.edu.cn (L.M.), z.yao@sjtu.edu.cn (Z.Y.), wujs@whut.edu.cn (J.W.)

https://doi.org/10.1016/j.xcrp.2023.101480

lattice at low voltage.[18,19] When the electrochemical voltage exceeds ~4.1 V, an abrupt anisotropic lattice contraction along the *c*-axis by as much as 5% (termed "lattice collapse," also known as "H2-H3" phase transition process.) has been identified for Ni-rich NCM, producing extensive mechanical strain. This strain leads to the generation of defects and pulverization of the cathode particles and a rapid performance decay upon cycling.[20–23] The increment of the Ni content makes the lattice collapse at a lower delithiation voltage,[23] and creates a more severe anisotropic lattice change and strain.[24–27] However, state-of-the-art modeling of planar gliding and crack generation still lacks a clear understanding of the relationship between the internal strain intrinsically arising from the electrochemical reactions (especially those related to lattice collapse) and the generation of planar gliding and microcracks. And operando observations can play the key role in unraveling the origin of the mechanical degradation.[28,29]

In this work, we analyzed dynamic structural evolution along with Li-ion extraction in single-crystalline Ni-rich cathodes using *in situ* scanning transmission electron microscopy (STEM); we observed consecutive lattice collapse and the formation of planar gliding. Lattice collapse induces multiple planar gliding in its way to extend along the *c*-axis. Using density functional theory (DFT) calculations, we find that, when lattice collapse occurs at high voltage, the Li extraction mode converts from the classic solid-solution mode to the layer-by-layer mode upon deep discharge. Planar gliding then enables to mitigate the interlayer compression caused by lattice collapse. Moreover, the origin of the microcracking is found to be closely related to the consecutive lattice collapse and planar gliding, as a result of the layer-by-layer delithiation. Our work discloses the origin of the mechanical degradation in internal Ni-rich NCM single crystals; it correlates lattice collapse, planar gliding, and intragranular microcracking under the layer-by-layer delithiation model. These analyses will provide insight into the structural modifications in next-generation layered cathode materials.

RESULTS AND DISCUSSION

Correlation between mechanical degradation and lattice collapse

This work uses single-crystalline Ni-rich NCM cathodes (the Ni/Co/Mn atomic ratio is 6:2:2, noted as NCM 622; Figures S1–S3) to investigate the intrinsic structural degradation mechanism. *In situ* high-energy X-ray diffraction (HEXRD) has been carried out to study the correlation between the lattice parameter change and the degree of delithiation during the charging process, where lattice collapse is identified. Figures 1A and 1B depict the galvanostatic charge/discharge profiles and the *in situ* HEXRD patterns corresponding to the (003) and (110) Bragg reflections. The (003) variation illustrates the lattice changes along the *c*-direction, while (110) represents the changes in the *a*-*b* plane. The shift of the (003) peak shows an initial mild increase, followed by a sudden plunge of the lattice parameter *c* (termed as lattice collapse). The (110) peak shows a continuous shift toward higher angles (decline of the lattice parameter) at low voltages and remains relatively stable at high voltages above 4.1 V. Indeed, lattice collapse initiates at ~4.1 V and continues with a large plunge of the *c* parameter from 4.2 to 4.5 V. A "peak broadening" phenomenon is also identified during lattice collapse, which was also reported in a previous study[23] (Figure S4), implying that a variant spacing of the (003) lattice plane occurs in deep lattice-collapse stage.

Increasing the high cutoff voltage can increase both the energy density and the power density of the battery, but at the price of deepening lattice collapse. We carried

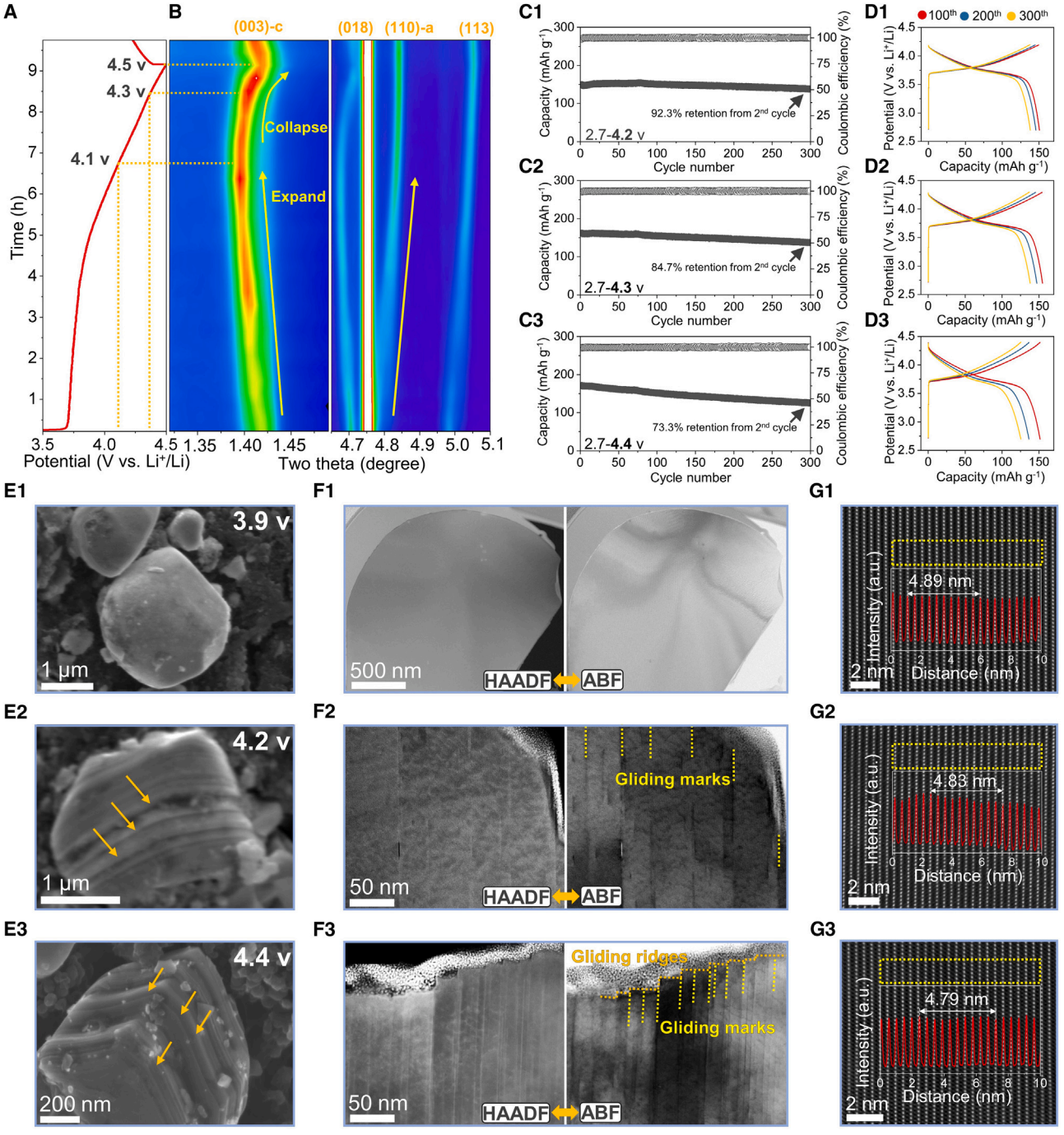

Figure 1. Correlating defect generation with lattice collapse in the single-crystalline Ni-rich cathode

(A and B) *In situ* HEXRD of the NCM/lithium half-cell. Voltage profile (A) and corresponding contour plot of the peak intensities (B).

(C1–C3) Cycling stability within different cutting off voltages.

(D1–D3) The corresponding charge-discharge curves of the half-cells in (C1)–(C3).

(E–G) *Ex situ* characterization of the NCM cathode. SEM images (E), cross-sectional HAADF/BF-STEM images along the [100] zone (F), and high-resolution HAADF-STEM images with the intensity profiles from labeled areas inset (G). The cathode was discharged to 3.9 V (E1, F1, and G1), 4.2 V (E2, F2, and G2) and 4.4 V (E3, F3, and G3).

out cycling measurements at elevated cutoff voltages at a current density of 60 mA g^{-1} (Figures 1C and 1D) to reveal the relation between the degree of lattice collapse and stability of the electrochemical performance. It is observed that as the cutoff voltage increases from 4.2 V to 4.3 and 4.4 V, the capacity retention at the 300th cycle drops from 92.3% to 84.7% and 73.3% with increased polarization over the cycles. It can be seen that as lattice collapse is deepened, the cyclability worsens, possibly because of a severer mechanical degradation.

The TEM data show that planar gliding and intragranular microcracks are formed in the cathodes that have undergone a lattice collapse. We characterized the microstructure of the charged Ni-rich NCM cathodes at an electrochemical voltage of 3.9 V (before lattice collapse) and 4.2 and 4.4 V (after lattice collapse) (Figures 1E–1G). At 3.9 V, the cathode has already experienced much electrochemical reaction, as a layer of rock-salt structure with the thickness of about 2 nm is found on the surface of the NCM 622 (Figure S5), which is ascribed to surface chemical degradation from aggravated redox reactions at the cathode-electrolyte interface. However, the particle remains intact with neither ridge appearing on the surface (Figure 1E1), nor gliding marks within its interior structure (Figure 1F1). The lattice spacing of the (003) planes, measured from the atomic-resolution STEM images, (Figure 1G1) is ~4.89 Å, confirming the expanded state compared with the pristine state (Figure S3E).

When charged to 4.2 and 4.4 V, many parallel and "sliced" ridges can be observed at the surface of the single crystal (Figures 1E2, 1E3, and S6). Planar gliding appears as white lines in the high-angle annular dark-field (HAADF)-STEM images and as black lines in the bright-field (BF)-STEM image (Figures 1F2 and 1F3). The lines (termed "gliding marks") are perpendicular to the *c*-axis and are caused by planar gliding in a model II-type crack (in-plane shear, according to fracture mechanics). The nature of the gliding mark is identified as a "strain caused diffraction contrast" (Figure S7; Note S1). Meanwhile, the edges of the ridges are mostly observed to be well aligned with the gliding marks (Figure S8; Note S2), implying both the ridges and gliding marks are all generated by planar gliding. The measured lattice spacing of the (003) planes is about ~4.83 and 4.79 Å at 4.2 and 4.4 V, respectively, which matches well with the *in situ* HEXRD results. Also, by comparing the density of gliding marks on the NCM particles at 4.2 and 4.4 V, we can conclude that the density of the defects has increased as the degree of lattice collapse is deepened.

When the electrochemical voltage is activated above 4.2 V, intragranular cracks are also observed. The cracks appear as narrow, dark strips parallel to the (003) planes, visible in the HAADF-STEM images (Figures S9 and S10); these cracks are formed by a parallel splitting of two adjacent TM layers. Note that both gliding marks and cracks do not appear at 3.9 V, but simultaneously appear at 4.2 and 4.4 V, showing their relationship with lattice collapse.

Direct observation of consecutive lattice collapse and formation of planar gliding by *in situ* STEM

We observed lattice collapse in NCM single crystals by *in situ* STEM (the experimental setup is shown in Figure 2A), showing the dynamic process of how lattice collapse occurs during delithiation. As shown in Video S1, an interface is identified and quickly moving across the NCM crystal upon delithiation, and the contrast of the crystal (left side of the interface) becomes bright/dark in HAADF/BF contrast as soon as the interface passes. The increased brightness in the HAADF-STEM image (*Z* contrast) is normally caused by an increased thickness or mass density. Here it shows an increased density due to lattice collapse of the (003) planes. The video

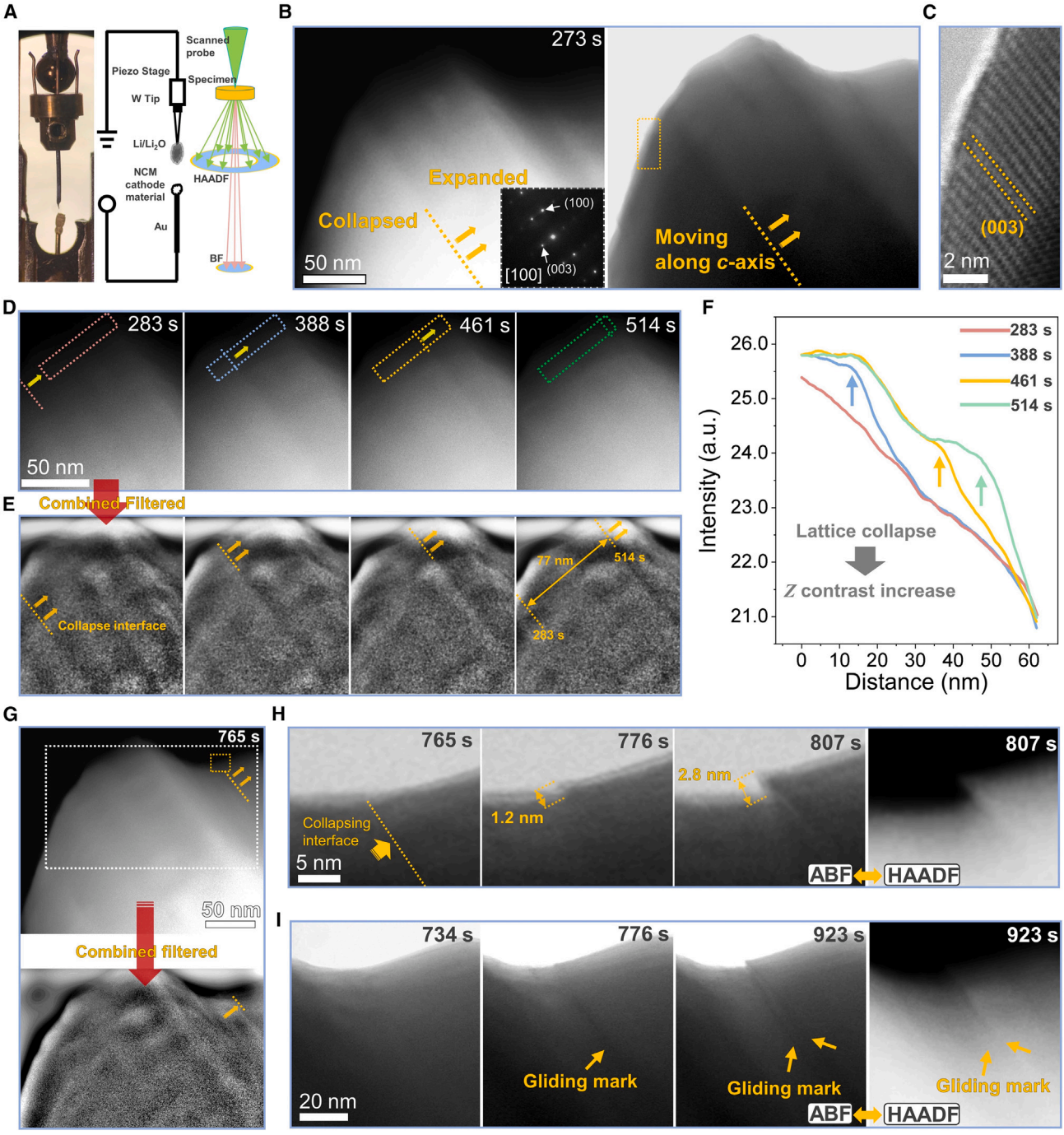

Figure 2. *In situ* STEM observed lattice collapse and generation of planar gliding

(A) Schematic illustration of the *in situ* HAADF/BF-STEM method.

(B) Representative time-lapse STEM image showing lattice collapse (inset: SAED pattern).

(C) Atomic-resolution BF-STEM image enlarged from the area marked by the rectangle in (B).

(D and E) Time-lapse HAADF-STEM images from Video S1 during *in situ* lithium extraction (D) and the corresponding filtered images (E).

(F) Intensity profiles from the areas labeled in (D) at different times.

(G) HAADF-STEM image and its filtered image before planar gliding.

(H) Time-lapse BF-STEM images enlarged from the area labeled by the yellow rectangle in (G) and HAADF-STEM image at 807 s on the right.

(I) Representative time-lapse BF-STEM images from Video S2 showing the generation process of planar gliding and HAADF-STEM image of 923 s on the right.

shows the consecutive lattice collapse taking place when Li and electrons are extracted. The consecutive lattice collapse could be identified by analyzing the intensity in the representative images extracted from the video during delithiation (Figures 2B–2F). The orientation of the crystal is close to the [100] orientation as shown by the inset in Figures 2B and 2C, where the orange dashed line parallel to the (003) planes marks the lattice-collapsing interface between the collapsed and the expanded (less collapsed) area. It is worth noting that for Ni-rich cathode, the collapsed area should be the H3 phase while the expanded area should be the H2 phase. Thus, the observed lattice collapsing process could be interpreted as the dynamic H2-H3 phase transition process, and the lattice-collapsing interface should therefore be assigned to the H2-H3 phase transition interface. To better visualize the collapsing interface, we used a combined "soft-rectangle" and band-pass filters to process the original HAADF images and compare with the BF images for a better contrast presentation (Figure S11; Note S3), where a lattice expansion process could also be identified before the collapse is initiated (Figure S12). The filtered images from 283 to 514 s (Figure 2E) show an obvious interface as marked by the yellow dashed line, where the interface has moved 77 nm along the *c*-axis at 231 s, with an average moving speed of ~0.33 nm s^{-1}.

By measuring the dynamic changes of the image intensity, a direct comparison between the collapsed and expanded (less-collapsed) region can be obtained during its movement (Figure 2F). The intensity profiles have been measured, starting from the same position, in a single-crystalline particle (marked by red, blue, orange, and green dashed rectangles in Figure 2D). All profiles exhibit an oblique trend with a similar slope, which is attributed to the change of thickness from the edge to the interior grain. Compared with the intensity profiles collected at 283 s, those collected at 388, 461, and 514 s indicate a gradual intensity increase from 0 to 60 nm as indicated by the blue, orange, and green arrows, respectively. The increase ratio of the intensity is similar to the lattice shrinkage of the (003) planes during lattice collapse (~2.5%), further proving the consecutive lattice collapse during delithiation (Figure S13; Note S4).

Besides the dynamic lattice collapse, we also observed the operando generation of a planar gliding. During the movement of the collapsing interface, four places are observed to have planar gliding generated exactly at the lattice collapsing interface (Figures 2G–2I and S14–S16), which is clearly seen in Video S2. Figure 2G shows the HAADF-STEM image and filtered image right before planar gliding is generated, when the collapse interface has moved to the position marked by the yellow dashed line. Figure 2I is the enlarged and time-lapse image from the area marked by the yellow dashed rectangle in Figure 2G. At 765 s, the surface of the particles is smooth and intact. In the next frame at 776 s, the surface of particle shows a small ridge with the right side rising by ~1.2 nm, which indicates that planar gliding is generated exactly at the collapsing interface. Moreover, at 807 s, further planar gliding occurs on the similar position, generating a new ridge with a height of 2.8 nm (Figure 2H). The gliding marks are also simultaneously generated with the ridges as marked by the yellow arrows in Figure 2I, which matches well with the *ex situ* results, confirming that both the ridge on the surface and the gliding mark inside are indeed signatures of planar gliding.

The layer-by-layer delithiation model and its correlation with lattice collapse and planar gliding by DFT calculations

The *in situ* STEM results, clearly indicate that the consecutive lattice-collapse model is different from the conventional uniform lattice contraction model (Figure 3A). In the uniform lattice contraction model, the lattice contracts as a whole, whereas in

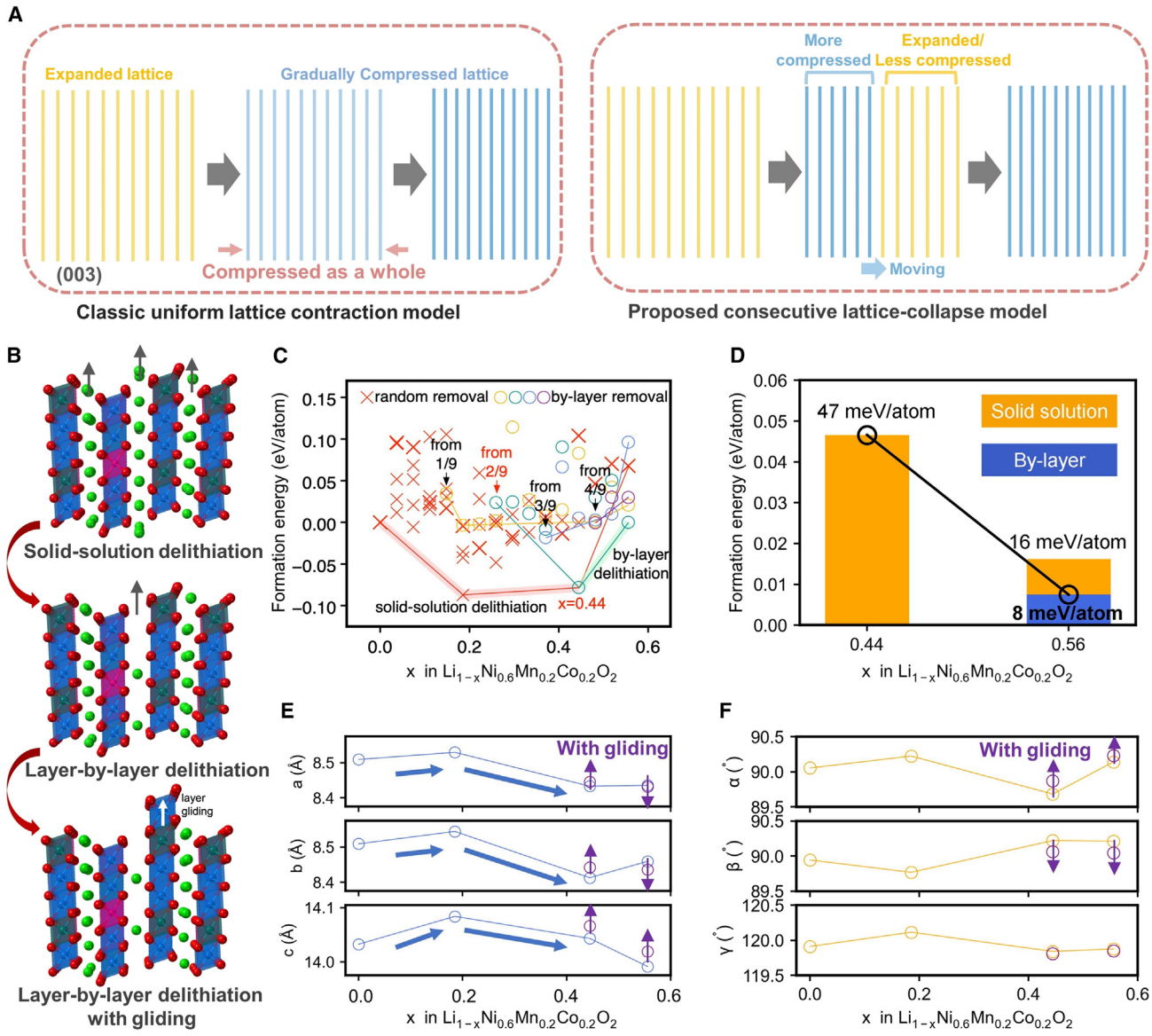

Figure 3. Establishment of the layer-by-layer delithiation model and its correlation with lattice collapse and planar gliding by DFT calculations

(A) Classical solid-solution delithiation mode versus the layer-by-layer delithiation mode.

(B) Illustration of the proposed delithiation path.

(C) Formation energy of each path at different delithiation stages.

(D) Formation energy of planar gliding at different delithiation stages.

(E and F) Lattice parameter variation at different delithiation stages.

the consecutive lattice-collapse model, the lattice contraction is initiated in one place, and then gradually extends in a "layer-by-layer" form until the whole crystal is contracted. As lattice collapse is generated by Li extraction at high voltage, a different type of delithiation mode (layer-by-layer delithiation) can also be considered and is supported by DFT first-principles calculations.

Such a calculation attempts to reveal the thermodynamic character of the layer-by-layer delithiation model and its correlation with the consecutive lattice collapse and planar gliding (Figure 3B). We have further illustrated this conversion from classic

solid solution delithiation to layer-by-layer delithiation in thermodynamic perspective: we calculated and compared the energy at various delithiation state through solid solution/layer-by-layer delithiation to explore an easiest delithiation route (Figure 3C). To simulate the conventional solid solution delithiation behavior, we started with an NCM $LiNi_{0.6}Mn_{0.2}Co_{0.2}O_2$ supercell (27 × 27 × 27) and randomly removed Li ions from the structure from $x = 0.0$ to $x = 0.56$ (charge ending point according to experiments). To simulate the layer-by-layer delithiation model and determine its exact initiation point, we started with the same supercell and randomly removed Li ions until a series of initiation points ($x = 0.11$, 0.22, 0.33, and 0.44, marked by yellow, green, blue, and purple circles, respectively) are reached. After these points, we removed Li preferentially from a single layer before we moved on to other layers until the endpoint ($x = 0.56$) is reached. These $Li_{1-x}Ni_{0.6}Mn_{0.2}Co_{0.2}O_2$ structures were all relaxed in DFT to have their total energies calculated. The corresponding formation energies were then evaluated referring to the pristine phase: $E_F = E(Li_{1-x}Ni_{0.6}Mn_{0.2}Co_{0.2}O_2) - E(LiNi_{0.6}Mn_{0.2}Co_{0.2}O_2) + x\mu(Li)$. Delithiation convex hulls of all these delithiation processes are constructed and by comparing their relative heights, we can identify the ground state delithiation reaction pathway. We observed a switch from the original randomized solid-solution Li removal delithiation behavior ($x = 0.11$, 0.22, and 0.3, at low voltage, during lattice expanding) to the layer-by-layer delithiation at a composition close to $x = 0.44$ (at high voltage, when lattice collapse happens), which is in agreement with the experiments. It is worth noting that layer-by-layer delithiation will naturally induce Li concentration gradient, which was thought to be the cause of planar gliding and crack in the previous study.[17]

To unravel the origin of planar gliding, planar gliding was introduced to the solid solution delithiated phase ($x = 0.44$, representing low-voltage delithiation) and both solid solution and layer-by-layer delithiated phases ($x = 0.56$, representing high-voltage delithiation) to study its thermodynamic impact on the delithiation process (Figure 3D). At $x = 0.44$, the formation energy for planar gliding is 47 meV/atom. For $x = 0.56$, the formation energy decreases to 16 meV/atom for the solid-solution mode and 8 meV/atom for the layer-by-layer delithiation mode. 8 meV/atom is a very low formation energy, which implies a high possibility of the generation of planar gliding upon deep-charge state in the layer-by-layer delithiation mode. Over the whole simulated delithiation period ($0.0 < x < 0.56$), we identified an initial increment of the lattice parameters *a*, *b*, and *c* ($0.0 < x < 0.19$) followed by a decrease ($0.19 < x < 0.56$), which matches with the HEXRD measurements (Figures 3E and 3F). The decrease of the *c*-axis is believed to be caused by the transfer of negative charge from O to TM atoms, which depletes the effective charge on oxygen at high state of charge and drastically reduces repulsion between the oxygen planes and hence the interlayer spacing (Li–O slabs).[23] We notice that the layer gliding will mitigate the interlayer compression (*c* decrement); this implies that the internal stress accumulated during the layer-by-layer delithiation can be released by planar gliding, as observed in TEM. We also observe a formation energy decrement at $x = 0.56$ for the Ni migration (from the transition metal layer to the Li layer) from 41 meV/atom (without layer gliding) to 20 meV/atom (with layer gliding). These results fit well with the TM anti-sites observed in the HAADF-STEM images (Figure S17; Note S5).

Mechanical degradation in Ni-rich layered cathode at high voltage

When Ni-rich NCM is electrochemically activated to a high voltage, the layer-by-layer delithiation induces consecutive lattice collapse, generating non-uniform strain as the triggering source of the mechanical degradation. The strain can then be released by the formation of not only planar gliding (Figure 4), but also intragranular microcracks (Figure 4A). The collapsed lattice and the expanded lattice have a difference in lattice

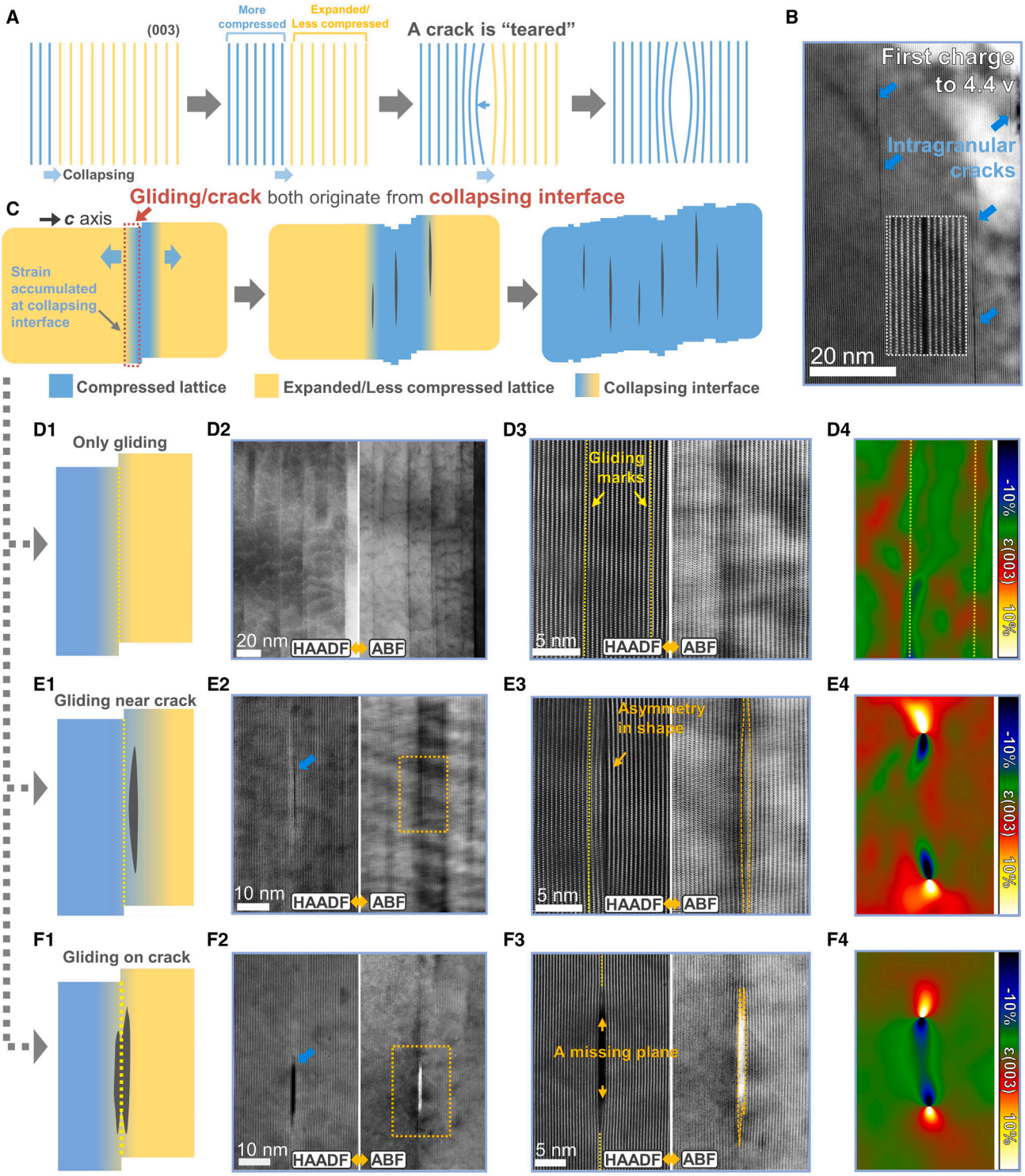

Figure 4. Generation of intragranular microcracks through the layer-by-layer delithiation model and its correlation with planar gliding

(A) Schematic illustration of the crack formation in the layer-by-layer delithiation model.

(B) Schematic illustration of planar gliding and microcrack generation during delithiation.

(C) Cross-sectional *ex situ* HAADF-STEM image of cathode first charged 4.4 V showing several intragranular microcracks.

(D–F) Different combos of planar gliding and microcracks: (D) planar gliding only, (E) planar gliding near a microcrack, (F) planar gliding on a microcrack. (D1, E1, and F1) Illustration of the defects and their reversibility. (D2, E2, and F2) HAADF/BF-STEM images. (D3, E3, and F3) High-resolution HAADF/BF-STEM images. (D4, E4, and F4) Strain (ε_{xx}) mappings calculated by GPA, from (D3), (E3), and (F3), respectively.

spacing (up to 5%), which induces intragranular tensile strain along the *c*-axis, and the collapsing interface will become the place where this strain is accumulated. Microcracks would be formed through (003) planes splitting (the plane is "teared") at the collapsing interface to release this strain within the cathode particle. The *in situ* observed crack generation in the collapsing interface is shown in Figure S18. In this defect generation model, the cracks are likely to be initiated from grain interior as observed from Figure 4B. Also, the "crack climbing" with adjacent crack formation could be accommodated in this model (Figure S19; Note S6).

The schematic illustration of the generation of planar gliding and microcracks are shown in Figure 4C: lattice collapse can be initiated in one or several areas in a cathode particle when a high discharge voltage (usually above 4.1 V) is reached, then gradually extend with the collapsing interface moving along the *c*-axis. And planar gliding and microcracking will be generated at the collapsing interface where the strain is accumulated. The influence of the polarization is also analyzed because of different current densities on the collapsing behavior and the formation of mechanical degradation (Figure S20; Note S7).

As planar gliding and microcracks have been demonstrated as important means of releasing the strain (because of consecutive lattice collapse), they are closely related and possibly mutually influenced. For instance, the strain can be released by merely planar gliding (Figure 4D), or planar gliding and a nearby microcrack (Figure 4E), or both planar gliding and the microcrack at the same location (Figure 4F). The representative HAADF/BF-STEM image (Figure 4D3), and its corresponding strain mapping (Figure 4D4) shows the strain distribution around planar gliding. When planar gliding mark is near, but not on the crack, the microcrack shows a typical asymmetric shape: the strain "bends" the microcrack toward the position of the gliding mark (Figure 4E3). The phenomenon is more obvious in the strain mapping (Figure 4E4). A microcrack near a gliding mark induces no material loss (the microcrack is formed by a parallel splitting of two adjacent TM layers), and therefore it provides possibilities for self-repairing during the subsequent cycling, and as such it could be reversible. However, when the microcrack is on the gliding mark (Figures 4F and S21), an obvious missing plane is observed in the middle of the microcrack, indicative of a material loss during the generation of the defect. This material loss will prohibit repairing the microcrack, and therefore microcracks on the gliding marks are most likely irreversible (because of repeated formation of the defects in the same location in cycling).

In summary, we show that in single-crystalline Ni-rich NCM cathodes, the layer-by-layer delithiation mode becomes dominant after lattice collapse is initiated at high electrochemical voltage. The consecutive lattice collapse generates a non-uniform and large strain in the collapsing interface, which is then released by the generation of planar gliding and microcracking. Although a single planar gliding or microcrack is reversible and can be repaired upon cycling, an overlay of planar gliding and microcracking will lead to the formation of irreversible cracks, which then causes the mechanical degradation of the Ni-rich cathodes within the internal grain. The consecutive lattice collapse is observed by *in situ* STEM, where the collapsing is initiated at one site and then consecutively extended. The DFT calculations confirm that the Li extraction mechanism will convert from the classic solid solution to a layer-by-layer path upon deep charging, where planar gliding enables to mitigate the interlayer strain. This work correlates the intrinsic structural phenomena, including lattice collapse, planar gliding, and intragranular microcracking within the consecutive lattice-collapse model; it provides insight into the structure modifications to be expected in next-generation layered cathode materials.

EXPERIMENTAL PROCEDURES

Resource availability

Lead contact

Further information and requests for resources should be directed to and will be fulfilled by the lead contact, Jinsong Wu (wujs@whut.edu.cn).

Materials availability

This study was performed with commercially available materials and did not generate new unique reagents.

Data and code availability

All data generated or analyzed during this study are included in this article (and its supplemental information files).

Electrochemical measurements

The single-crystalline NCM cathode was provided by Tianjin B&M Science and Technology prepared from solid reaction method. The electrochemical properties were tested by the assembling CR2016-type coin cells with Li metal foil as the anode in Ar atmosphere. The cathodes were composed of 80% active material, 10% polyvinylidene difluoride (PVDF), and 10% acetylene black. A solution (1.0 M) of $LiPF_6$ in ethyl carbonate/dimethyl carbonate/ethyl methyl carbonate (EC/DMC/EMC = 1:1:1 vol %) was used as the electrolyte. Al foil is used as the collector. The mass loading of each electrode was 4–5 mg cm^{-2}. Galvanostatic charge/discharge measurement was carried out on a multichannel battery testing system (LAND CT2001A). To prepare the sample after cycling for *ex situ* SEM and TEM characterization, the electrode was charged in a very small current density (10 mA g^{-1}) to avoid polarization, then the electrodes were taken out of the disassembled cell and then soaked in acetone for 48 h to remove the residual electrolyte.

Material characterization

In situ HEXRD patterns were collected at beamline 11-ID-C of Advanced Photon Source at Argonne National Laboratory, with a beam with a size of 0.2 × 0.2 mm^2 and wavelength of 0.1173 Å. Coin cells were cycled at 20 mA g^{-1} between 2.7 and 4.5 V using a MACCOR cycler. During the cell cycling, the HEXRD patterns were collected every 600 s, using a Perkin-Elmer two-dimensional (2D) X-ray detector. The 2D diffraction patterns were then converted into 1D patterns of 2θ versus intensity using GSAS-II software calibrated against a CeO_2 standard. The STEM images and EDX spectra were collected using a CEOS probe corrected FEI Themis TEM (electron accelerating voltage is 300 kV). The probe convergence angle was 17.8 mrad, at a probe current of ~45 pA for STEM imaging and EDS acquisition. For *in situ* STEM, a miniature battery was built inside the electron microscope, with cathode material on the gold tip as the cathode and Li metal attached to the surface of the tungsten needle as the anode. The Li_2O from the surface oxidation of the Li metal serves as the solid electrolyte. The bias was slowly increased from 0 V to ~4.5 V with the rate of ~0.2 V/s and mains at 4.5 V for Li extraction when Li_2O reached the cathode material. Performing STEM with both HAADF and BF detectors allows us to collect dark field and BF images simultaneously, and use their combined advantages. Each frame in the recorded video is ~10.5 s. Such an *in situ* STEM method using the *in situ* solid open cell could achieve high-resolution imaging. However, the solid-state lithiation environment could only resemble, but not replicate, the real battery condition.

First-principles calculations

All DFT calculations reported in this study were performed using the Vienna Ab-initio Simulation Package (VASP)[30–33] with the projector augmented wave (PAW) potentials[34] and the Perdew-Becke-Ernzerhof (PBE)[35] exchange correlation. A plane wave basis with a cutoff energy of 520 eV and Γ-centered *k*-meshes with a density of 8,000 *k*-points per reciprocal atom was used for all calculations. All calculations were spin-polarized, with Mn and Ni atoms initialized in high-spin configurations and Co atoms initialized in low-spin configurations.[36,37] They were all relaxed to self-consistency. The DFT + *U* method introduced by Dudarev et al.[38] was used to treat the localized 3*d* electrons of Mn, Ni, and Co with *U* of 3.8, 6.4, and 3.3 obtained by fitting it to experimental and calculated formation enthalpies in a previous study.[39]

SUPPLEMENTAL INFORMATION

Supplemental information can be found online at https://doi.org/10.1016/j.xcrp.2023.101480.

ACKNOWLEDGMENTS

This work was supported by the National Natural Science Foundation of China (52072282, 52150710537, 52127816, and 51832004) and the National Key R&D Program of China (2022YFB3803501).

AUTHOR CONTRIBUTIONS

J.W. and L.M. conceived the project. R.Y. did structure characterization, *in situ*/*ex situ* STEM characterization, and electrochemical characterization and analyzed the results. W.Z. helped test the electrochemical performance. Z.Y. performed DFT calculations. J.W. and G.V.T. supervised the TEM studies and analyzed the results. L.Z. supervised electrochemical test. All authors discussed the results and commented on the manuscript.

DECLARATION OF INTERESTS

The authors declare no competing interests.

Received: January 17, 2023
Revised: April 19, 2023
Accepted: June 9, 2023
Published: June 30, 2023

REFERENCES

1. Li, W., Song, B., and Manthiram, A. (2017). High-voltage positive electrode materials for lithium-ion batteries. Chem. Soc. Rev. *46*, 3006–3059.

2. Manthiram, A., Knight, J.C., Myung, S.T., Oh, S.M., and Sun, Y.K. (2016). Nickel-rich and lithium-rich layered oxide cathodes: progress and perspectives. Adv. Energy Mater. *6*, 1501010.

3. Yan, P., Zheng, J., Zhang, J.-G., and Wang, C. (2017). Atomic resolution structural and chemical imaging revealing the sequential migration of Ni, Co, and Mn upon the battery cycling of layered cathode. Nano Lett. *17*, 3946–3951.

4. Xu, K. (2014). Electrolytes and interphases in Li-ion batteries and beyond. Chem. Rev. *114*, 11503–11618.

5. Amatucci, G., Tarascon, J., and Klein, L. (1996). Cobalt dissolution in $LiCoO_2$-based non-aqueous rechargeable batteries. Solid State Ionics *83*, 167–173.

6. Min, S.H., Jo, M.R., Choi, S.Y., Kim, Y.I., and Kang, Y.M. (2016). A layer-structured electrode material reformed by a PO_4-O_2 hybrid framework toward enhanced lithium storage and stability. Adv. Energy Mater. *6*, 1501717.

7. Lin, F., Nordlund, D., Li, Y., Quan, M.K., Cheng, L., Weng, T.-C., Liu, Y., Xin, H.L., and Doeff, M.M. (2016). Metal segregation in hierarchically structured cathode materials for high-energy lithium batteries. Nat. Energy *1*, 15004–15008.

8. Bi, Y., Tao, J., Wu, Y., Li, L., Xu, Y., Hu, E., Wu, B., Hu, J., Wang, C., Zhang, J.-G., et al. (2020). Reversible planar gliding and microcracking in a single-crystalline Ni-rich cathode. Science *370*, 1313–1317.

9. Zhang, F., Lou, S., Li, S., Yu, Z., Liu, Q., Dai, A., Cao, C., Toney, M.F., Ge, M., Xiao, X., et al. (2020). Surface regulation enables high stability of single-crystal lithium-ion cathodes at high voltage. Nat. Commun. *11*, 3050.

10. Ulvestad, A., Singer, A., Cho, H.-M., Clark, J.N., Harder, R., Maser, J., Meng, Y.S., and Shpyrko, O.G. (2014). Single particle nanomechanics in

operando batteries via lensless strain mapping. Nano Lett. *14*, 5123–5127.

11. Yan, P., Zheng, J., Gu, M., Xiao, J., Zhang, J.-G., and Wang, C.-M. (2017). Intragranular cracking as a critical barrier for high-voltage usage of layer-structured cathode for lithium-ion batteries. Nat. Commun. *8*, 14101–14109.

12. Qian, G., Zhang, Y., Li, L., Zhang, R., Xu, J., Cheng, Z., Xie, S., Wang, H., Rao, Q., He, Y., et al. (2020). Single-crystal nickel-rich layered-oxide battery cathode materials: synthesis, electrochemistry, and intra-granular fracture. Energy Storage Mater. *27*, 140–149.

13. Singer, A., Zhang, M., Hy, S., Cela, D., Fang, C., Wynn, T.A., Qiu, B., Xia, Y., Liu, Z., Ulvestad, A., et al. (2018). Nucleation of dislocations and their dynamics in layered oxide cathode materials during battery charging. Nat. Energy *3*, 641–647.

14. Lee, E.-J., Chen, Z., Noh, H.-J., Nam, S.C., Kang, S., Kim, D.H., Amine, K., and Sun, Y.-K. (2014). Development of microstrain in aged lithium transition metal oxides. Nano Lett. *14*, 4873–4880.

15. Miller, D.J., Proff, C., Wen, J.G., Abraham, D.P., and Bareño, J. (2013). Observation of microstructural evolution in Li battery cathode oxide particles by in situ electron microscopy. Adv. Energy Mater. *3*, 1098–1103.

16. Nadimpalli, S.P., Sethuraman, V.A., Abraham, D.P., Bower, A.F., and Guduru, P.R. (2015). Stress evolution in lithium-ion composite electrodes during electrochemical cycling and resulting internal pressures on the cell casing. J. Electrochem. Soc. *162*, A2656–A2663.

17. Ulvestad, A., Singer, A., Clark, J.N., Cho, H.M., Kim, J.W., Harder, R., Maser, J., Meng, Y.S., and Shpyrko, O.G. (2015). Topological defect dynamics in operando battery nanoparticles. Science *348*, 1344–1347.

18. Zhou, Y.-N., Ma, J., Hu, E., Yu, X., Gu, L., Nam, K.-W., Chen, L., Wang, Z., and Yang, X.-Q. (2014). Tuning charge–discharge induced unit cell breathing in layer-structured cathode materials for lithium-ion batteries. Nat. Commun. *5*, 5381–5388.

19. Dolotko, O., Senyshyn, A., Mühlbauer, M., Nikolowski, K., and Ehrenberg, H. (2014). Understanding structural changes in NMC Li-ion cells by in situ neutron diffraction. J. Power Sources *255*, 197–203.

20. Kondrakov, A.O., Schmidt, A., Xu, J., Geßwein, H., Mönig, R., Hartmann, P., Sommer, H., Brezesinski, T., and Janek, J. (2017). Anisotropic lattice strain and mechanical degradation of high-and low-nickel NCM cathode materials for Li-ion batteries. J. Phys. Chem. C *121*, 3286–3294.

21. Liu, H., Wolfman, M., Karki, K., Yu, Y.-S., Stach, E.A., Cabana, J., Chapman, K.W., and Chupas, P.J. (2017). Intergranular cracking as a major cause of long-term capacity fading of layered cathodes. Nano Lett. *17*, 3452–3457.

22. Lee, W., Muhammad, S., Kim, T., Kim, H., Lee, E., Jeong, M., Son, S., Ryou, J.H., and Yoon, W.S. (2018). New insight into Ni-rich layered structure for next-generation Li rechargeable batteries. Adv. Energy Mater. *8*, 1701788.

23. Li, W., Asl, H.Y., Xie, Q., and Manthiram, A. (2019). Collapse of $LiNi_{1-x-y}Co_xMn_yO2$ lattice at deep charge irrespective of Nickel content in Lithium-ion batteries. J. Am. Chem. Soc. *141*, 5097–5101.

24. Ishidzu, K., Oka, Y., and Nakamura, T. (2016). Lattice volume change during charge/discharge reaction and cycle performance of Li $[Ni_xCo_yMn_z]O_2$. Solid State Ionics *288*, 176–179.

25. Sun, H.-H., and Manthiram, A. (2017). Impact of microcrack generation and surface degradation on a nickel-rich layered Li $[Ni_{0.9}Co_{0.05}Mn_{0.05}]O_2$ cathode for lithium-ion batteries. Chem. Mater. *29*, 8486–8493.

26. Ryu, H.-H., Park, K.-J., Yoon, C.S., and Sun, Y.-K. (2018). Capacity fading of Ni-rich $Li[Ni_xCo_yMn_{1-x-y}]O_2$ $(0.6 \leq x \leq 0.95)$ cathodes for high-energy-density lithium-ion batteries: bulk or surface degradation? Chem. Mater. *30*, 1155–1163.

27. Li, J., Shunmugasundaram, R., Doig, R., and Dahn, J.R. (2016). In situ X-ray diffraction study of layered Li–Ni–Mn–Co oxides: effect of particle size and structural stability of core–shell materials. Chem. Mater. *28*, 162–171.

28. Wang, H., Liu, F., Yu, R., and Wu, J. (2022). Unraveling the reaction mechanisms of electrode materials for sodium-ion and potassium-ion batteries by in situ transmission electron microscopy. Interdisciplinary Materials *1*, 196–212.

29. Yu, R., Pan, Y., Liu, Y., Zhou, L., Zhao, D., Wu, J., and Mai, L. (2023). Constructing sub 10 nm scale interfused TiO_2/SiO_x bicontinuous hybrid with mutual-stabilizing effect for lithium storage. ACS Nano *17*, 2568–2579.

30. Kresse, G., and Hafner, J. (1993). Ab initio molecular dynamics for liquid metals. Phys. Rev. B *47*, 558–561.

31. Kresse, G., and Hafner, J. (1994). Ab initio molecular-dynamics simulation of the liquid-metal–amorphous-semiconductor transition in germanium. Phys. Rev. B *49*, 14251–14269.

32. Kresse, G., and Furthmüller, J. (1996). Efficient iterative schemes for ab initio total-energy calculations using a plane-wave basis set. Phys. Rev. B *54*, 11169–11186.

33. Kresse, G., and Furthmüller, J. (1996). Efficiency of ab-initio total energy calculations for metals and semiconductors using a plane-wave basis set. Comput. Mater. Sci. *6*, 15–50.

34. Blöchl, P. (1994). Projector augmented-wave method. Phys. Rev. B *50*, 17953–17979.

35. Perdew, J.P., Ernzerhof, M., and Burke, K. (1996). Rationale for mixing exact exchange with density functional approximations. J. Chem. Phys. *105*, 9982–9985.

36. Yao, Z., Chan, M.K.Y., and Wolverton, C. (2022). Exploring the origin of anionic redox activity in super Li-rich iron oxide-based high-energy-density cathode materials. Chem. Mater. *34*, 4536–4547.

37. Yao, Z., Kim, S., He, J., Hegde, V.I., and Wolverton, C. (2018). Interplay of cation and anion redox in $Li_4Mn_2O_5$ cathode material and prediction of improved $Li_4(Mn, M)_2O_5$ electrodes for Li-ion batteries. Sci. Adv. *4*, eaao6754.

38. Dudarev, S.L., Botton, G.A., Savrasov, S.Y., Humphreys, C.J., and Sutton, A.P. (1998). Electron-energy-loss spectra and the structural stability of nickel oxide: an LSDA+ U study. Phys. Rev. B *57*, 1505–1509.

39. Wang, L., Maxisch, T., and Ceder, G. (2006). Oxidation energies of transition metal oxides within the GGA+ U framework. Phys. Rev. B *73*, 195107.